

LoRA-PT: Low-Rank Adapting UNETR for Hippocampus Segmentation

Using Principal Tensor Singular Values and Vectors

Guanghua He^{1,2}, Wangang Cheng², Hancan Zhu² and Gaohang Yu^{1*}

¹ Department of Mathematics, Hangzhou Dianzi University, Hangzhou, 310018, China

² School of Mathematics, Physics and Information, Shaoxing University, Shaoxing, 312000, China

* Corresponding author: Gaohang Yu, E-mail address: maghyu@163.com

Abstract

The hippocampus is a crucial brain structure associated with various psychiatric disorders, and its automatic and precise segmentation is essential for studying these diseases. In recent years, deep learning-based methods have made significant progress in hippocampus segmentation. However, training deep neural network models requires substantial computational resources and time, as well as a large amount of labeled training data, which is often difficult to obtain in medical image segmentation. To address this issue, we propose a new parameter-efficient fine-tuning method called LoRA-PT. This method transfers the pre-trained UNETR model on the BraTS2021 dataset to the hippocampus segmentation task. Specifically, the LoRA-PT method categorizes the parameter matrix of the transformer structure into three sizes, forming three 3D tensors. Through tensor singular value decomposition, these tensors are decomposed to generate low-rank tensors with the principal singular values and singular vectors, while the remaining singular values and vectors form the residual tensor. During the fine-tuning, we only update the low-rank tensors, i.e. the principal tensor singular values and vectors, while keeping the residual tensor unchanged. We validated the proposed method on three public hippocampus datasets. Experimental results show that LoRA-PT outperforms existing parameter-efficient fine-tuning methods in segmentation accuracy while significantly reducing the number of parameter updates. Our code is available at <https://github.com/WangangCheng/LoRA-PT/tree/LoRA-PT>.

Keywords: parameter-efficient fine-tuning, tensor singular value decomposition, hippocampus segmentation, deep learning

1. Introduction

The hippocampus is a crucial brain structure, closely associated with cognitive functions such as memory and spatial navigation. In neuroimaging research and clinical applications, morphological changes in the hippocampus are key biomarkers for neurodegenerative diseases like Alzheimer’s disease, making precise segmentation essential for quantitative analysis and pathological studies [1-3]. However, accurate automated segmentation of the hippocampus remains challenging due to its complex anatomical structure, indistinct boundaries, and low contrast with surrounding tissues. These factors are compounded by significant anatomical variability among individuals, particularly under pathological conditions, making it difficult for generic segmentation algorithms to consistently perform well across different cases. In recent years, deep learning methods have made significant progress in the field of medical image segmentation [4-6]. Nonetheless, these methods still face limitations when applied to hippocampus

segmentation. Deep learning models typically require a large volume of labeled data for training. However, annotating medical images is both time-consuming and labor-intensive, making it challenging to acquire sufficient labeled data. Additionally, training these models requires substantial computational resources, which poses a significant limitation for research institutions and clinical settings with limited computational capabilities [7].

Transfer learning leverages knowledge acquired from training a model in one domain to enhance learning efficiency and performance in a related domain, while reducing the demand for data and computational resources to some extent [8, 9]. Traditional transfer learning methods typically fine-tune all parameters of the pre-trained model, which still requires substantial computational resources and training time and is prone to overfitting. To address these issues, parameter-efficient fine-tuning (PEFT) methods have emerged [10]. PEFT reduces the number of parameter updates by adjusting only a small portion of the model’s parameters, thereby improving fine-tuning efficiency and model performance. Recently, a PEFT method called LoRA has been proposed and rapidly advanced [11]. This method performs a low-rank approximation on the parameter matrix of the pre-trained model and updates only the low-rank section of the parameters during fine-tuning.

Deep neural network models process the input features layer by layer, with correlations between the parameters of each layer. For example, the UNETR model [12] has an encoder branch consisting of 12 sequentially stacked transformer layers, through which the input features pass in order. Consequently, the transformer matrices of different layers are highly correlated. When these transformer matrices are concatenated into a tensor, the resulting tensor exhibits low-rank properties. Building on this analysis, we extend LoRA to the tensor form and propose a new PEFT method based on the tensor Singular Value Decomposition (t-SVD), named LoRA-PT. Specifically, we categorize the parameter matrices of the transformer’s structure into three different sizes, forming three 3D tensors, and decompose them using the t-SVD. The decomposition splits the tensor into a principal low-rank part and a residual part. During the fine-tuning, we keep the residual tensor frozen and update only the low-rank tensor.

Using the proposed LoRA-PT method, we adapt the UNETR model pre-trained on the BraTS2021 dataset to hippocampus segmentation. Experimental results show that with a small number of training samples (e.g., 10 training samples), the average Dice score of the LoRA-PT method across three datasets improved by 1.36% compared to the full-tuning method, HD95 decreased by 0.294, and the number of updated parameters was only 3.16% of those in full-tuning. Additionally, LoRA-PT outperforms existing PEFT methods in segmentation accuracy, including LoRA [11], LoTR [13], and PISSA [14].

The main advantages of the LoRA-PT method are as follows:

- Compared to the LoRA method, which decomposes and fine-tunes each matrix individually, LoRA-PT uses the t-SVD to decompose and fine-tune the tensor formed by the parameter matrices of different layers, effectively leveraging the overall low-rank structure of the model.
- The LoRA-PT method initializes the low-rank tensor using principal tensor singular values and vectors, and enhances information interaction between parameters of different layers during the fine-tuning through tensor computation, facilitating overall model optimization.
- We applied the LoRA-PT method to transfer the UNETR model pre-trained on the BraTS2021 dataset to hippocampus image segmentation, and the results showed that the performance of the LoRA-PT method surpassed several state-of-the-art EPTL methods.

2. Related work

2.1 Tensor decomposition

Tensor decomposition is an essential tool for multi-dimensional data analysis, widely used in signal processing, machine learning, and chemometrics. These methods reveal the intrinsic structure of data and improve processing efficiency by decomposing tensors into lower-dimensional representations. Common tensor decomposition methods include CANDECOMP/PARAFAC (CP) decomposition, Tucker decomposition, tensor train decomposition (TT decomposition), and t-SVD [15, 16]. CP decomposition breaks down a tensor into a sum of rank-one tensors and is commonly used for analyzing multi-channel data, such as in chemometrics and multi-channel signal analysis in neuroscience [17]. Tucker decomposition breaks a tensor into a core tensor multiplied by a set of orthogonal matrices, making it suitable for image analysis, video processing, and multi-dimensional statistics [18]. TT decomposition simplifies data storage and computation by breaking high-dimensional tensors into a series of smaller three-dimensional tensors [19]. T-SVD, based on matrix singular value decomposition, is effective for data compression and recovery [20].

In recent years, the application of tensor decomposition methods has expanded in fields like computer vision. Cichocki et al. explored the use of tensor networks in dimensionality reduction and large-scale optimization, analyzing their practical applications and future potential in machine learning, data analysis, and the physical sciences [21]. Chang and Wu proposed a tensor-based multi-relational signal processing least squares method, improving the efficiency and accuracy of multi-dimensional data analysis with applications in network security, bioinformatics, and social network analysis [22]. Qiu et al. studied a noise tensor completion method based on the low-rank structure of Tensor Ring (TR), optimizing the processing of large-scale, high-dimensional data [23]. Kong et al. introduced a new tensor recovery technique based on the low Tubal-rank assumption, enhancing the efficiency and accuracy of multi-dimensional data recovery through a multi-layer subspace prior learning mechanism, making it suitable for image processing and video completion [24]. These studies demonstrate the broad application of tensor decomposition methods in multi-dimensional data processing and their significant potential in improving data analysis efficiency and accuracy.

2.2 Deep learning for hippocampus segmentation

Deep learning has significantly advanced hippocampus image segmentation. Lin et al. proposed a 3D multi-scale multi-attention U-Net for hippocampus segmentation, enhancing accuracy and robustness by combining multi-scale features and attention mechanisms [25]. Liu et al. developed a multi-model deep convolutional neural network for hippocampus segmentation and classification in Alzheimer's disease [6]. Shi et al. introduced a dual dense context-aware network, integrating dense features and contextual information to improve segmentation accuracy and robustness [26]. Yang et al. presented CAST, a multi-scale convolutional neural network toolkit for automated hippocampal subfield segmentation, achieving precise results through multi-scale feature extraction and convolutional neural network techniques [27]. Goubran et al. conducted a study using a three-dimensional convolutional neural network specifically for hippocampus segmentation in brains with extensive atrophy, overcoming the limitations of traditional methods in handling brain tissue atrophy caused by diseases [28]. Zhu et al. proposed a dilated dense U-Net model for infant hippocampal subfield segmentation, effectively improving the recognition of fine and complex structures in infant hippocampal subfields by combining dilated convolutions and densely connected network structures [29]. He et al. introduced a deep convolutional neural network for hippocampus segmentation, which particularly enhances boundary refinement by incorporating a boundary refinement module into the network architecture, significantly improving the segmentation accuracy of hippocampal edges, thus making the overall segmentation results more accurate and reliable [4].

Additionally, transfer learning methods, which adjust pre-trained model parameters to accelerate training, have been applied to hippocampus segmentation. Ataloglou et al. proposed a rapid and accurate hippocampus segmentation method combining deep convolutional neural network ensembles and transfer learning [30]. Balboni et al. explored the impact of transfer learning on 3D deep convolutional neural networks for hippocampus segmentation in patients with mild cognitive impairment and Alzheimer’s disease [31]. Transfer learning strategies enabled the model to achieve higher segmentation accuracy and efficiency when processing complex brain imaging data with cognitive impairment characteristics. This work shows that transfer learning can enhance the model’s adaptability to disease-specific changes, providing an effective approach for hippocampus segmentation and aiding early diagnosis and research of Alzheimer’s disease. Van Opbroek et al. introduced a transfer learning method using feature space transformation for hippocampus segmentation across different scanning devices. This method addresses inconsistencies in image features caused by device differences by mapping features from one scanner’s feature space to another [32]. These studies indicate that transfer learning can effectively improve the accuracy and consistency of hippocampus segmentation across different scanning devices.

2.3 Parameter-efficient fine-tuning

Unlike traditional transfer learning methods, PEFT methods transfer models by adjusting only a small portion of the pre-trained model’s parameters. This significantly reduces the reliance on large amounts of labeled data and computational resources. Houlsby et al. introduced the Adapter module, embedding a small number of trainable parameters into the pre-trained transformer model, allowing it to adapt to new tasks while keeping most parameters fixed [10]. Mou et al. proposed T2i-adapter, designed specifically for text-to-image diffusion models, aiming to improve the controllability of generative models [33]. Zhang et al.’s Llama-adapter utilizes a zero-initialized attention mechanism for efficient fine-tuning [34]. Li and Liang proposed Prefix-tuning, which optimizes a small number of parameters to adjust the prefix part of the model, significantly reducing the parameters needed for fine-tuning [35].

Hu et al. developed Low-Rank Adaptation (LoRA), which adjusts pre-trained models by applying low-rank matrix decomposition to their weight matrices without disrupting their original structure [11]. Chen et al. proposed SuperLoRA, optimizing multi-layer attention modules to enhance model performance while maintaining parameter efficiency [36]. Liu et al.’s Dora method achieves PEFT through weight decomposition and low-rank adaptation, optimizing storage and computational efficiency [37]. Si et al.’s FLoRA method, designed for N-dimensional data, projects data into a low-rank core space for data compression and feature extraction, improving data processing and training efficiency [38]. Kopiczko et al. proposed Vera, enhancing model performance by adjusting random matrices in the model structure based on vector strategies [39]. Bershtatsky et al. introduced the LoTR technique, optimizing model weights through tensor low-rank adaptation using tensor Tucker decomposition, reducing parameter count and improving computational efficiency [13]. Jie and Deng’s Fact method, designed for lightweight adaptation of vision transformer models, selectively adjusts key factors using TT and Tucker decomposition, enhancing performance on specific visual tasks [40]. Meng et al. proposed the PISSA method, focusing on adapting the principal singular values and vectors of large language models for efficient fine-tuning [14].

These methods achieve fine-tuning in various ways, enhancing model adaptability and performance while reducing computational and storage demands, making them suitable for a wide range of deep learning applications. However, there is currently limited research on parameter-efficient fine-tuning methods that incorporate tensor decomposition. In this paper, we propose a t-SVD-based PEFT method

that effectively leverages the low-rank structure of neural network tensors for parameter compression. Moreover, by initializing the low-rank tensors with principal tensor singular values and vectors, our method facilitates the optimization process during the fine-tuning phase.

3. Method

UNETR consists of an encoder path and a decoder path. The encoder path is constructed by stacking 12 transformers, while the decoder path is composed of convolution layers, batch normalization, and ReLU activation functions. The encoder and decoder are connected through deconvolution, convolution, batch normalization, and ReLU activation functions. Detailed information on the UNETR structure can be found in the original literature [12]. Since most parameters in UNETR are concentrated in the transformer structure, our proposed LoRA-PT method fine-tunes the parameters of the transformer structure, keeps the parameters of the decoder path fully updated, and freezes the parameters of the modules in the long skip connection path. The framework of the LoRA-PT method is shown in Figure 1, divided into three parts: tensorization of UNETR, t-SVD of tensors, and extraction and fine-tuning of principal tensor singular values and vectors.

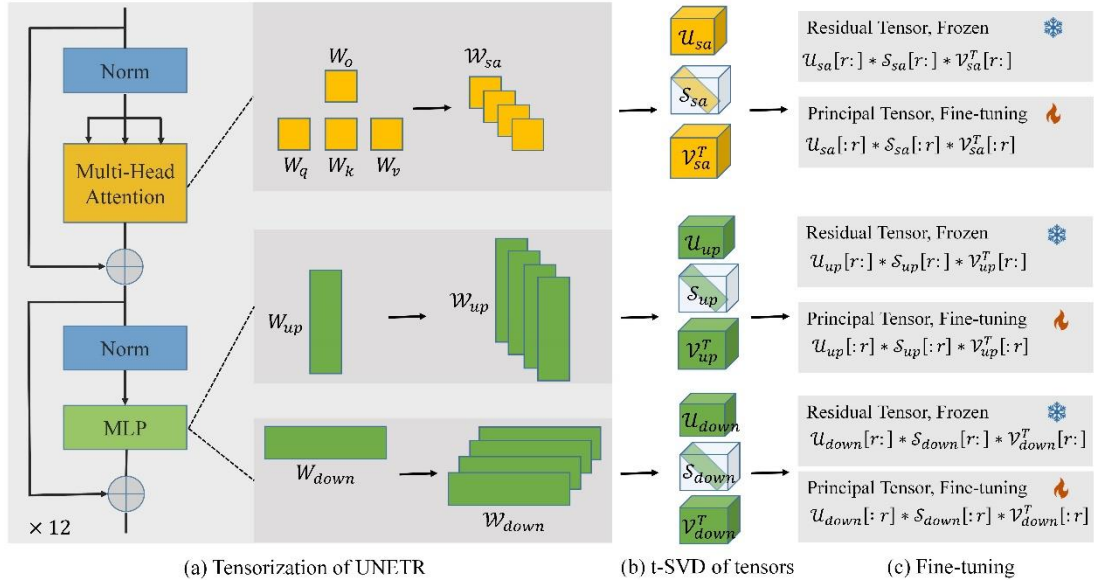


Figure 1. Schematic diagram of the LoRA-PT method framework. (a) The encoder part of UNETR is tensorized into three tensors of different sizes: $\mathcal{W}_{sa}, \mathcal{W}_{up}, \mathcal{W}_{down}$. (b) The tensors $\mathcal{W}_{sa}, \mathcal{W}_{up}, \mathcal{W}_{down}$ are decomposed using the t-SVD. (c) Principal tensor singular values and vectors are extracted and fine-tuned.

3.1 Tensorization of UNETR

Tensorizing a neural network involves representing the network's parameters using tensors. The transformer layers in the UNETR network consist of two types of modules: Multi-Head Self-Attention (MHSA) and Multi-Layer Perceptron (MLP). In MHSA, the query, key, value, and output are parameterized by matrices $W_q, W_k, W_v, W_o \in R^{d \times d}$. These transformations are further divided into N_h heads: $W_q^{(i)}, W_k^{(i)}, W_v^{(i)}, W_o^{(i)}, i = 1, 2, \dots, N_h$. Thus, MHSA can be expressed by the following formula:

$$MHSA(X) = \sum_{i=1}^{N_h} \text{softmax}\left(\frac{XW_q^{(i)}W_k^{(i)T}X^T}{\sqrt{d}}\right)XW_v^{(i)}W_o^{(i)T}.$$

An MLP module consists of two fully connected (FC) layers. For simplicity, ignoring the bias parameters, the formula for the MLP is:

$$MLP(X) = GELU(XW_{up})W_{down},$$

where $W_{up} \in R^{d \times 4d}$ and $W_{down} \in R^{4d \times d}$ are the weights of the FC layers.

Based on the above analysis, each transformer layer contains four $d \times d$ matrices in the MHSA module, and one $d \times 4d$ matrix and one $4d \times d$ matrix in the MLP module. Since UNETR includes 12 transformer layers, there are a total of 48 $d \times d$ matrices, 12 $d \times 4d$ matrices, and 12 $4d \times d$ matrices. As shown in Figure 1(a), we concatenate the 48 $d \times d$ matrices to form the tensor \mathcal{W}_{sa} , concatenate the 12 $d \times 4d$ matrices to form the tensor \mathcal{W}_{up} , and concatenate the 12 $4d \times d$ matrices to form the tensor \mathcal{W}_{down} . Here, $\mathcal{W}_{sa} \in R^{d \times d \times 48}$, $\mathcal{W}_{up} \in R^{d \times 4d \times 12}$ and $\mathcal{W}_{down} \in R^{4d \times d \times 12}$.

3.2 Tensor singular value decomposition

The t-SVD is an important tool for processing tensor (multi-dimensional array) data. The core idea of the t-SVD is to extend the concept of matrix Singular Value Decomposition (SVD) to higher-order tensors, representing a complex tensor as the tensor product (t-Product) of three simpler tensors. Below, we first introduce the concept of the t-Product [20].

Definition1. (t-Product) Let $\mathcal{A} \in R^{n_1 \times n_2 \times n_3}$ and $\mathcal{B} \in R^{n_2 \times l \times n_3}$ be two third-order tensors, the t-Product $\mathcal{A} * \mathcal{B}$ is a tensor with the size of $n_1 \times l \times n_3$,

$$\mathcal{A} * \mathcal{B} = \text{fold}(\text{circ}(\mathcal{A})\text{MatVec}(\mathcal{B})),$$

where

$$\text{circ}(\mathcal{A}) = \begin{bmatrix} A_1 & A_{n_3} & \cdots & A_2 \\ A_2 & A_1 & \cdots & A_3 \\ \vdots & \vdots & \ddots & \vdots \\ A_{n_3} & A_{n_3-1} & \cdots & A_1 \end{bmatrix}$$

and

$$\text{MatVec}(\mathcal{B}) = \begin{bmatrix} B_1 \\ B_2 \\ \vdots \\ B_{n_3} \end{bmatrix}$$

where $A_i = \mathcal{A}(:, :, i)$, $B_i = \mathcal{B}(:, :, i)$, $i = 1, 2, \dots, n_3$ are the frontal slices of \mathcal{A} and \mathcal{B} respectively, the operation "fold" takes $\text{MatVec}(\mathcal{B})$ back to tensor \mathcal{B} , i.e. $\text{fold}(\text{MatVec}(\mathcal{B})) = \mathcal{B}$.

It is known that block circulant matrices can be block diagonalized by the discrete Fourier transform (DFT) [20, 41]. Specifically,

$$(F \otimes I_{n_1})\text{circ}(\mathcal{A})(F^* \otimes I_{n_2}) = \begin{bmatrix} \hat{A}_1 & 0 & \cdots & 0 \\ 0 & \hat{A}_2 & \cdots & 0 \\ \vdots & \vdots & \ddots & \vdots \\ 0 & 0 & \cdots & \hat{A}_{n_3} \end{bmatrix},$$

where $F \in R^{n_3 \times n_3}$ is the DFT matrix, F^* is the conjugate transpose of F , \otimes is the Kronecker product, I_{n_1} is the identity matrix of size $n_1 \times n_1$, I_{n_2} is the identity matrix of size $n_2 \times n_2$, and \hat{A}_i are the frontal slices of $\hat{\mathcal{A}}$, which is the Fast Fourier Transform (FFT) of \mathcal{A} along the third mode. Given that,

$$\text{circ}(\mathcal{A})\text{MatVec}(\mathcal{B}) = (F^* \otimes I_{n_1})((F \otimes I_{n_1})\text{circ}(\mathcal{A})(F^* \otimes I_{n_2}))(F \otimes I_{n_2})\text{MatVec}(\mathcal{B}),$$

to compute $\mathcal{A} * \mathcal{B}$, we apply the FFT on tensors \mathcal{A} and \mathcal{B} along the third mode, perform matrix multiplication on each two-dimensional slice of the transformed tensors, and finally apply the inverse FFT along the third mode to obtain the final tensor. With the t-Product defined, we now introduce t-SVD.

Definition2. (t-SVD) Let $\mathcal{A} \in R^{n_1 \times n_2 \times n_3}$, then \mathcal{A} can be factored as

$$\mathcal{A} = \mathcal{U} * \mathcal{S} * \mathcal{V}^T,$$

where \mathcal{U}, \mathcal{V} are orthogonal tensors with the size of $n_1 \times n_1 \times n_3$ and $n_2 \times n_2 \times n_3$ respectively, \mathcal{S} is a f-diagonal tensor with the size of $n_1 \times n_2 \times n_3$, and \mathcal{V}^T is the tensor transpose of \mathcal{V} . The t-SVD can be implemented using the FFT, with specific details available in reference [20].

3.3 Principal tensor singular values and vectors extraction and fine-tuning

As shown in Figure 1(b), we perform the t-SVD on the three obtained tensors \mathcal{W}_{sa} , \mathcal{W}_{up} and \mathcal{W}_{down} respectively,

$$\begin{aligned}\mathcal{W}_{sa} &= \mathcal{U}_{sa} * \mathcal{S}_{sa} * \mathcal{V}_{sa}^T, \\ \mathcal{W}_{up} &= \mathcal{U}_{up} * \mathcal{S}_{up} * \mathcal{V}_{up}^T, \\ \mathcal{W}_{down} &= \mathcal{U}_{down} * \mathcal{S}_{down} * \mathcal{V}_{down}^T,\end{aligned}$$

where,

$$\begin{aligned}\mathcal{U}_{sa} &\in R^{d \times d \times 48}, \mathcal{S}_{sa} \in R^{d \times d \times 48}, \mathcal{V}_{sa} \in R^{d \times d \times 48}, \\ \mathcal{U}_{up} &\in R^{d \times d \times 12}, \mathcal{S}_{up} \in R^{d \times 4d \times 12}, \mathcal{V}_{up} \in R^{4d \times 4d \times 12}, \\ \mathcal{U}_{down} &\in R^{4d \times 4d \times 12}, \mathcal{S}_{down} \in R^{4d \times d \times 12}, \mathcal{V}_{down} \in R^{d \times d \times 12}.\end{aligned}$$

Using the results of the t-SVD, we extract r principal tensor singular values and vectors, as shown in Figure 1(c). Taking \mathcal{W}_{sa} as an example, the left r principal tensor vectors are $\mathcal{U}_{sa}[:, :r, :]$, the right r principal tensor vectors are $\mathcal{V}_{sa}^T[:, :r, :]$ and r principal tensor values are $\mathcal{S}_{sa}[:, :r, :]$. We then represent tensor \mathcal{W}_{sa} as the sum of a principal low-rank tensor and a residual tensor,

$$\mathcal{W}_{sa} = \mathcal{W}_{sa}^{PT} + \mathcal{W}_{sa}^{Res}.$$

Here, \mathcal{W}_{sa}^{PT} is the principal low-rank tensor, obtained by the t-Product of principal tensor singular values and vectors, i.e. $\mathcal{W}_{sa}^{PT} = \mathcal{U}_{sa}[:, :r, :] * \mathcal{S}_{sa}[:, :r, :] * \mathcal{V}_{sa}^T[:, :r, :]$, and \mathcal{W}_{sa}^{Res} is the residual tensor, obtained by the t-Product of residual tensor singular values and vectors, i.e. $\mathcal{W}_{sa}^{Res} = \mathcal{U}_{sa}[:, :r, :] * \mathcal{S}_{sa}[:, :r, :] * \mathcal{V}_{sa}^T[:, :r, :]$.

In the above, r is the number of principal tensor singular values and vectors, and is also the tensor tubal rank of \mathcal{W}_{sa}^{PT} , where $r \ll d$. Similar to the LoRA method [11], during the fine-tuning stage, we keep the residual tensor \mathcal{W}_{sa}^{Res} fixed and only update the principal low-rank tensor \mathcal{W}_{sa}^{PT} . For efficient storage, we avoid storing the tensor \mathcal{W}_{sa}^{PT} during fine-tuning. Instead, we store the principal tensor singular values and vectors $\mathcal{U}_{sa}[:, :r, :]$, $\mathcal{S}_{sa}[:, :r, :]$ and $\mathcal{V}_{sa}^T[:, :r, :]$.

4. Experiments

4.1 Datasets

4.1.1 The Dataset for pre-training

The UNETR model is first pre-trained on the BraTS2021 dataset [42]. The BraTS2021 dataset is an important resource in the field of brain tumor segmentation, consisting of multi-modal magnetic resonance imaging (MRI) data, including four imaging modalities: T1, T1ce, T2, and FLAIR. The imaging data for each patient has a resolution of $240 \times 240 \times 155$, with a voxel size of $1 \times 1 \times 1$ mm³. The BraTS2021 dataset provides detailed tumor region annotations for 1,251 cases, with annotation

categories including Enhancing Tumor (ET), Peritumoral Edema/Infiltrating Tissue (ED), and Necrotic Tumor Core (NCR).

4.1.2 Hippocampus datasets

We applied the LoRA-PT method to transfer the pre-trained UNETR model to hippocampus segmentation and validated it on three hippocampus datasets: the EADC-ADNI dataset [43], the LPBA40 dataset [44], and the HFH dataset [45].

The EADC-ADNI dataset, sourced from the ADNI database (<http://adni.loni.usc.edu/>), contains MR images of 135 patients, with an image resolution of $197 \times 233 \times 189$ and a voxel size of $1 \times 1 \times 1$ mm³. The hippocampus annotations for each image were provided by the EADC-ADNI (European Alzheimer's Disease Consortium and Alzheimer's Disease Neuroimaging Initiative) harmonized segmentation protocol (www.hippocampal-protocol.net) [43]. After careful inspection, we found that the hippocampus annotations and images of five patients did not match, so we excluded those cases.

The LPBA40 dataset, created by the Laboratory of Neuro Imaging (LONI) in Los Angeles, is a valuable resource for neuroimaging research. This dataset contains 3D brain MRI scans of 40 healthy adults, with image dimensions of $256 \times 124 \times 256$ and a voxel size of $0.8938 \times 1.500 \times 0.8594$ mm³. Each scan is precisely annotated, covering 56 brain tissues and anatomical structures. We extracted the hippocampus region to validate our method.

The HFH dataset includes 50 T1-weighted MRI brain images from two different MRI vendors, with varying resolutions and contrasts. The image dimensions are $256 \times 124 \times 256$ and $512 \times 124 \times 512$, with voxel sizes of $0.781 \times 2.000 \times 0.781$ mm³ and $0.39 \times 2.00 \times 0.39$ mm³, respectively. Since only 25 images provided hippocampus annotations, we conducted experiments with these 25 annotated images.

For the above three hippocampus datasets, we used FSL to register all images to the MNI152 standard space and performed standard preprocessing procedures, including skull stripping, resampling, and affine transformation. The processed image resolution is $182 \times 218 \times 182$ with a voxel size of $1 \times 1 \times 1$ mm³.

4.2 Evaluation metrics

We chose the Dice coefficient and Hausdorff Distance 95% (HD95) as evaluation metrics. The Dice coefficient measures the relative overlap volume between the automatic segmentation and the ground truth, defined as:

$$Dice = 2 \frac{V(A \cap B)}{V(A) + V(B)},$$

where A represents the ground truth, B represents the automatic segmentations, and $V(S)$ represents the volume of S . Hausdorff Distance 95% (HD95) is a robust version of the Hausdorff distance, used to evaluate the robustness of the segmentation structure and the consistency of the segmentation boundaries, defined as:

$$HD95(A, B) = \max(h_{95}(A, B), h_{95}(B, A)),$$

where $h_{95}(A, B) = K_{a \in A, b \in B}^{95} \min d(a, b)$ is the 95th ranked minimum Euclidean distance between boundary points in A and B .

4.3 Implementation details

We conducted experiments using the PyTorch framework on two NVIDIA GeForce RTX 4090D GPUs. During the pre-training process, we merged the three annotated regions of the BraTS2021 dataset

into a single tumor region for segmentation. We used only the T1ce modality data as input to the network and divided the 1,251 publicly annotated cases into training, validation, and test sets in a ratio of 1000:125:126. Training parameters were set according to the original paper [12].

During the fine-tuning process, we used the Adam optimizer with a batch size of 4 and adopted a poly learning rate strategy. The initial learning rate was set to 0.001, decaying by a power of 0.9 with each iteration. We extracted image patches of size $128 \times 128 \times 128$ as network input using random cropping and applied several data augmentation strategies, including: (1) random mirroring with a probability of 0.5 along the axial, coronal, and sagittal planes; (2) random intensity shift, adding or subtracting a random value within $[-0.1, 0.1]$ to each voxel’s intensity; and (3) randomly scaling the image within a range of $[0.9, 1.1]$. The network’s loss function was Dice loss, defined as follows:

$$\mathcal{L}(Y, \tilde{Y}) = -\frac{1}{N} \sum_{n=1}^N \frac{2Y_n \tilde{Y}_n}{Y_n + \tilde{Y}_n},$$

where Y_n and \tilde{Y}_n represent the ground truth and predicted probability, respectively, and N is the batch size. The loss function includes the L2 norm for regularization, with a weight decay rate of 10^{-5} . The network was trained for a total of 1000 epochs.

During the testing phase, we extracted image patches of size $128 \times 128 \times 128$ and used a non-overlapping sliding window strategy to input them into the trained model for segmentation. We averaged the results of the last four epochs to obtain the final inference result. In the post-processing stage, we removed false positive hippocampus regions through the following steps: create a binary mask to identify all connected target regions, define a threshold of 1000 mm^3 , and remove all connected regions smaller than this threshold by setting their labels to background. This approach reduces model errors and noise, thereby improving segmentation performance.

5. Results

We compared the proposed LoRA-PT method with existing fine-tuning methods, including Full tuning, Linear-probing, LoRA[11], Adapter[46], SSF[47], LoTR[13], and PISSA[14]. Full tuning refers to updating all parameters. Linear-probing updates all the linear layers in the transformer block. LoRA decomposes the model’s weight matrices into low-rank matrices, and during the fine-tuning stage, only the parameters of the low-rank matrices are updated. Adapter uses structural reparameterization techniques to optimize visual models, enhancing efficiency and reducing computational complexity. SSF introduces scaling and rotation factors after each operation in the transformer, updating only the introduced parameters while keeping the rest frozen. LoTR adapts neural network weights using Tucker tensor decomposition. PISSA adapts neural network models by adjusting the principal singular values and singular vectors. In Section 4.3.1, we first select the hyper-parameter rank r for different methods; in Section 4.3.2, we compare and analyze the results of different methods.

5.1 Selection of optimal rank

The rank r , as a hyper-parameter, is crucial in LoRA, Adapter, LoTR, PISSA, and our proposed LoRA-PT method. We randomly selected five samples from the EADC-ADNI dataset as the training set, with the remaining samples used as the test set. We conducted experiments with these methods under different rank settings ($r \in \{1, 2, 4, 8, 16, 32\}$). Table 1 lists the Dice values of segmentation results for different methods under various ranks. From the table, it can be seen that the optimal rank is $r = 32$ for LoRA and Adapter, $r = 2$ for LoTR and PISSA, and $r = 1$ for LoRA-PT. In subsequent experiments, unless otherwise specified, we use these optimal rank values.

Table 1. Dice values (\uparrow) of segmentation results for different fine-tuning methods with various ranks on the EADC-ADNI dataset. The best results are highlighted in bold.

Method	$r=1$	$r=2$	$r=4$	$r=8$	$r=16$	$r=32$
LoRA	84.28	84.00	83.64	84.06	84.10	84.35
Adapter	83.58	83.80	83.91	83.49	83.74	84.08
LoTR	83.83	84.05	83.85	83.63	83.67	83.50
PISSA	84.16	84.25	83.91	83.68	83.91	83.86
LoRA-PT	84.47	83.72	83.83	83.61	83.84	83.69

5.2 Comparison with state-of-the-art methods

We conducted fine-tuning experiments with small sample sizes, randomly selecting five or ten samples from each of the three hippocampus datasets for training. Tables 2 and 3 present the segmentation results of different methods on the three datasets with five and ten training samples, respectively. In terms of the number of learned parameters, the proposed LoRA-PT method requires 2.8445M parameters, comparable to SSF, LoTR, and PISSA, and only 3.16% of the parameters required by the Full tuning method. This significantly reduces the number of parameters to be learned, enhancing training efficiency. Despite the high training efficiency, the LoRA-PT method also achieved high-precision hippocampus segmentation. With five training samples, using Full tuning as the baseline, the LoRA-PT method improved the average Dice score by 1.22% and reduced HD95 by 0.168 across the three datasets. With ten training samples, using Full tuning as the baseline, the LoRA-PT method improved the average Dice score by 1.36% and reduced HD95 by 0.294 across the three datasets.

Across all three datasets, regardless of whether five or ten training samples were used, the proposed LoRA-PT method consistently achieved the highest segmentation performance based on the Dice coefficient. It not only outperformed the LoRA method but also exceeded the performance of the recently introduced LoTR and PISSA methods. For the HD95 metric, the LoRA-PT method delivered the best results in all datasets, with the sole exception of the HFH dataset.

Table 2. Segmentation results on three hippocampus datasets with Dice and HD95 as evaluation metrics. *Five* samples were randomly selected as the training set, with the remaining samples used as the test set. The best results are highlighted in bold.

Method	Params (M)	EADC-ADNI		LPBA40		HFH	
		Dice \uparrow	HD95 \downarrow	Dice \uparrow	HD95 \downarrow	Dice \uparrow	HD95 \downarrow
Full tuning	90.0112	83.79	5.839	79.91	7.175	79.65	5.526
Linear-probing	59.3477	83.46	5.344	80.62	6.483	79.92	5.629
LoRA	7.3971	84.35	5.334	80.17	6.618	80.15	5.535
Adapter	7.9869	84.08	5.663	79.72	6.793	80.38	5.441
SSF	2.8828	83.73	5.326	79.08	6.904	78.33	6.378
LoTR	2.7033	84.05	5.394	80.21	7.011	79.88	5.762
PISSA	2.9736	84.25	5.604	80.52	6.584	79.71	5.848
LoRA-PT	2.8445	84.47	5.311	81.83	6.495	80.70	5.620

Table 3. Segmentation results on three hippocampus datasets with Dice and HD95 as evaluation metrics. *Ten* samples were randomly selected as the training set, with the remaining samples used as the test set.

The best results are highlighted in bold.

Method	Params (M)	EADC-ADNI		LPBA40		HFH	
		Dice \uparrow	HD95 \downarrow	Dice \uparrow	HD95 \downarrow	Dice \uparrow	HD95 \downarrow
Full tuning	90.0112	84.74	5.183	82.37	6.481	83.24	4.966
Linear-probing	59.3477	84.85	4.916	81.36	6.640	83.17	5.303
LoRA	7.3971	85.08	5.242	82.12	6.426	83.81	5.165
Adapter	7.9869	84.76	5.110	81.94	6.286	83.67	4.766
SSF	2.8828	84.79	5.034	80.69	7.090	81.57	5.271
LoTR	2.7033	85.90	4.654	82.70	6.453	83.69	5.027
PISSA [14]	2.9736	86.44	4.614	82.64	6.481	83.88	4.769
LoRA-PT	2.8445	86.50	4.436	83.52	6.251	84.40	5.060

We randomly selected one segmentation result from each of the three datasets to display, as shown in Figure 2. In Figure 2, each row shows the segmentation results obtained by different fine-tuning methods. For each segmentation result, both 2D slice images and 3D surface renderings are displayed. The blue regions indicate the overlap between the automatic segmentation results and the ground truth, while the pink regions show the areas where the automatic segmentation results and the ground truth do not match. From the figure, it is evident that the results obtained by the proposed LoRA-PT method are closer to the ground truth compared to other segmentation methods.

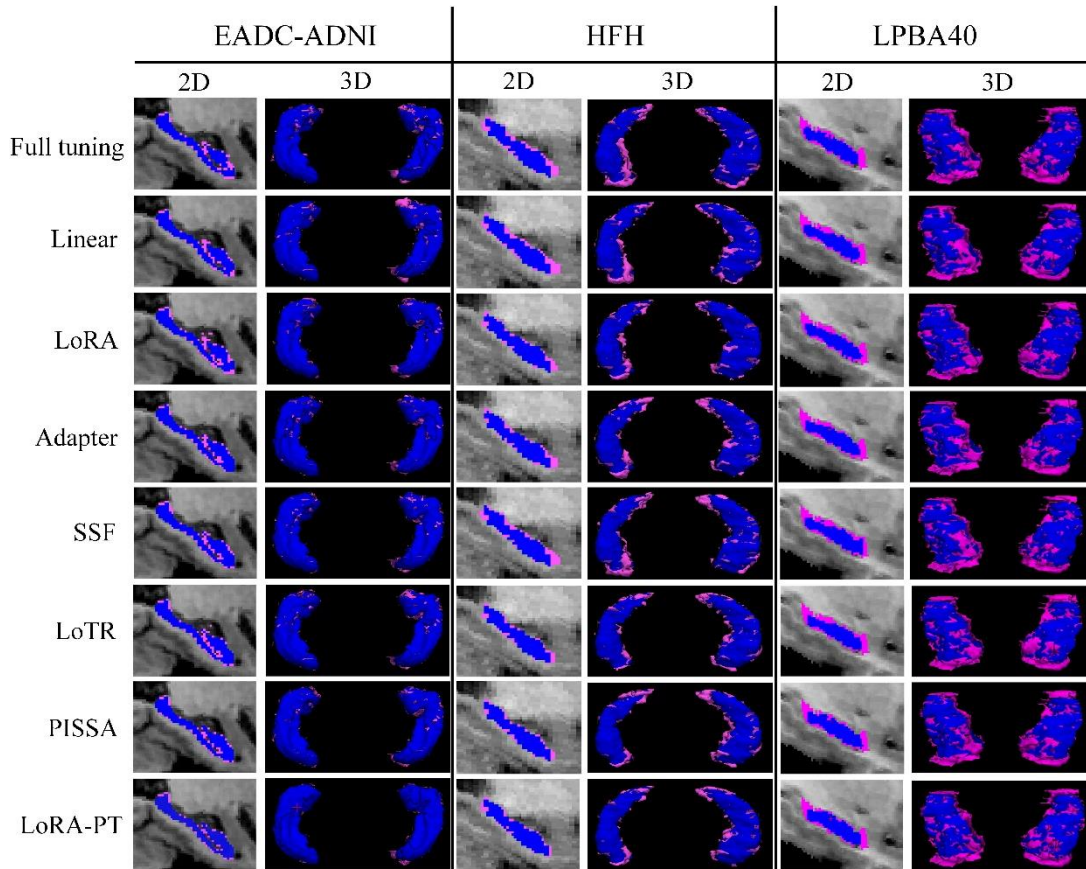


Figure 2. Segmentation results with ten training samples. A randomly selected segmentation result from each of the three datasets is displayed. For each result, both 2D slice images and 3D surface renderings are shown. The blue regions indicate the overlap between the automatic segmentation results and the

ground truth, while the pink regions indicate the areas where the automatic segmentation results and the ground truth do not match.

6. Discussion

The LoRA method reduces the number of parameters and computational complexity in the model transfer learning process by decomposing the weight matrices of the pre-trained model into low-rank matrices [11]. The PISSA method enhances LoRA by adjusting the principal singular values and singular vectors for model transfer learning [14]. PISSA not only adopts the concept of low-rank decomposition but also further utilizes information from principal singular values and singular vectors. This allows the model to adapt more efficiently to new tasks while maintaining performance and further reducing computational complexity. Similarly, the LoTR method improves upon LoRA by employing tensor Tucker decomposition techniques to adapt the neural network weights, further reducing the number of parameters and computational demands [13]. As seen in Table 1, the PISSA and LoTR methods achieve optimal performance at rank $r = 2$, while the LoRA method reaches optimal performance at rank $r = 32$. This indicates that adjusting the principal singular values and singular vectors, as well as utilizing tensor decomposition techniques, can effectively leverage the structural information of model parameters, thereby enhancing the performance of PEFT methods.

Our proposed LoRA-PT method builds on the aforementioned three methods by further leveraging the structural information of model parameters. Specifically, we use the t-SVD to break down the parameter tensor into a principal low-rank tensor (corresponding to the principal singular values and singular vectors in the PISSA method) and a residual tensor, updating only the low-rank tensor during fine-tuning. In fact, we extend the PISSA method from a matrix form to a higher-dimensional tensor form, thus more effectively utilizing the high-dimensional structural information of model parameters. Although both the LoTR method and our LoRA-PT method use tensor decomposition, the LoTR method does not effectively use the principal singular values and singular vectors for updating model parameters. Table 1 shows that our LoRA-PT method achieves optimal performance at rank $r = 1$, indicating that LoRA-PT can maximally utilize the structural information of model parameters for fine-tuning. Moreover, Tables 2 and 3 demonstrate that the LoRA-PT method outperforms the LoTR and PISSA methods in segmentation accuracy.

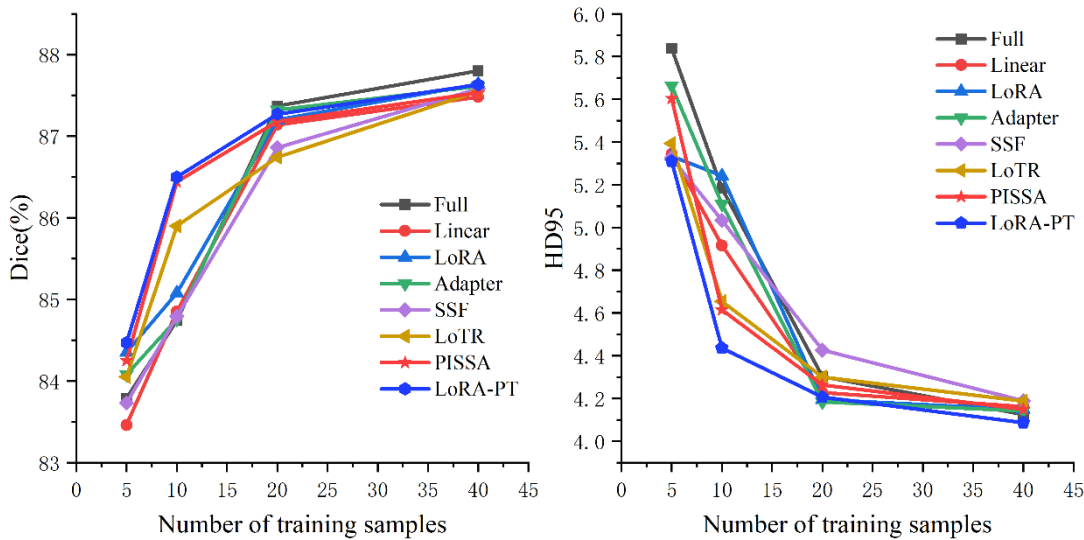


Figure 3. Comparison of accuracy for different fine-tuning methods with varying training sample sizes on the EADC-ADNI dataset. The left graph shows the analysis using the Dice coefficient, while the right

graph shows the analysis using HD95.

To illustrate the impact of training data quantity on fine-tuning methods, we conducted experiments on the EADC-ADNI dataset using different methods under varying amounts of training data. The results are shown in Figure 3. As shown in the figure, the segmentation accuracy gap between different fine-tuning methods narrows as the amount of data increases. From the Dice coefficient perspective (left graph of Figure 3), when the training data size is less than 20, the LoRA-PT and PISSA methods show superior segmentation performance. When the training data size exceeds 20, the Full tuning method outperforms all PEFT methods. This indicates that PEFT methods have an advantage in small sample scenarios. Additionally, the proposed LoRA-PT method maintains an advantage over other PEFT methods across different data sizes. In the right graph of Figure 3, similar results are shown using the HD95 metric. However, under the HD95 metric, the Full tuning method does not surpass some PEFT methods, including our LoRA-PT method, even when the training data size exceeds 20.

7. Conclusion

We proposed a novel parameter-efficient fine-tuning method based on the t-SVD, called LoRA-PT. Using the LoRA-PT method, we successfully transferred the UNETR model from the BraTS2021 dataset to the hippocampus segmentation task and validated its effectiveness on three public datasets. Experimental results demonstrate that our method significantly improves both performance and parameter efficiency. The LoRA-PT method includes a hyper-parameter rank r . In our experiments, we manually selected the optimal rank, which somewhat limits the efficiency of the optimization process. Future research could focus on developing methods for dynamically adjusting the rank to further improve the optimization efficiency and adaptability of the model. In future work, we plan to apply the LoRA-PT method to more datasets and tasks to further validate its generality and practicality.

CRedit authorship contribution statement

Guanghua He: Drafted the manuscript and conducted data analysis; Wangang Cheng: Developed the programming implementation; Hancan Zhu: Revised the manuscript and designed the algorithm; Gaohang Yu: Proposed the methodology and provided overall guidance.

Declaration of competing interest

The authors declare no financial interests or personal relationships that could have influenced this work.

Acknowledgments

Gaohang Yu's work was supported in part by National Natural Science Foundation of China (No. 12071104), Hancan Zhu's work was supported by Humanities and Social Science Fund of the Ministry of Education of China (No. 23YJAZH232) and Guanghua He's work was supported by Scientific Research Project of Shaoxing University (No. 20210038).

References

- [1] H. Zhu, S. Wang, L. Qu, and D. Shen, "Hippocampus segmentation in MR images: Multiatlas methods and deep learning methods," in *Big Data in Psychiatry# x0026; Neurology*: Elsevier, 2021, pp. 181-215.
- [2] M. P. Hosseini, M. R. Nazem-Zadeh, D. Pompili, K. Jafari-Khouzani, K. Elisevich, and H.

- Soltanian-Zadeh, "Comparative performance evaluation of automated segmentation methods of hippocampus from magnetic resonance images of temporal lobe epilepsy patients," *Medical physics*, vol. 43, no. 1, pp. 538-553, 2016.
- [3] Q. Zheng, Y. Zhang, H. Li, X. Tong, and M. Ouyang, "How segmentation methods affect hippocampal radiomic feature accuracy in Alzheimer's disease analysis?," *European Radiology*, vol. 32, no. 10, pp. 6965-6976, 2022.
- [4] G. He, G. Zhang, L. Zhou, and H. Zhu, "Deep convolutional neural network for hippocampus segmentation with boundary region refinement," *Medical & biological engineering & computing*, vol. 61, pp. 2329-2339, 2023.
- [5] J. V. Manjón, J. E. Romero, and P. Coupe, "A novel deep learning based hippocampus subfield segmentation method," *Scientific Reports*, vol. 12, no. 1, pp. 1-9, 2022.
- [6] M. Liu *et al.*, "A multi-model deep convolutional neural network for automatic hippocampus segmentation and classification in Alzheimer's disease," *NeuroImage*, vol. 208, p. 116459, 2020.
- [7] T. Lei, R. Wang, Y. Wan, B. Zhang, H. Meng, and A. K. Nandi, "Medical image segmentation using deep learning: a survey," *arXiv preprint arXiv:2009.13120*, 2021.
- [8] H. E. Kim, A. Cosa-Linan, N. Santhanam, M. Jannesari, M. E. Maros, and T. Ganslandt, "Transfer learning for medical image classification: a literature review," *BMC medical imaging*, vol. 22, no. 1, p. 69, 2022.
- [9] A. Van Opbroek, H. C. Achterberg, M. W. Vernooij, and M. De Bruijne, "Transfer learning for image segmentation by combining image weighting and kernel learning," *IEEE transactions on medical imaging*, vol. 38, no. 1, pp. 213-224, 2018.
- [10] N. Hounsby *et al.*, "Parameter-efficient transfer learning for NLP," in *International conference on machine learning*, 2019: PMLR, pp. 2790-2799.
- [11] E. J. Hu *et al.*, "Lora: Low-rank adaptation of large language models," *arXiv preprint arXiv:2106.09685*, 2021.
- [12] A. Hatamizadeh *et al.*, "Unetr: Transformers for 3d medical image segmentation," *Proceedings of the IEEE/CVF Winter Conference on Applications of Computer Vision*, pp. 574-584, 2022.
- [13] D. Bershtsky, D. Cherniuk, T. Daulbaev, and I. Oseledets, "LoTR: Low tensor rank weight adaptation," *arXiv preprint arXiv:2402.01376*, 2024.
- [14] F. Meng, Z. Wang, and M. Zhang, "Pissa: Principal singular values and singular vectors adaptation of large language models," *arXiv preprint arXiv:2404.02948*, 2024.
- [15] T. G. Kolda and B. W. Bader, "Tensor decompositions and applications," *SIAM review*, vol. 51, no. 3, pp. 455-500, 2009.
- [16] Y. Liu, J. Liu, Z. Long, and C. Zhu, *Tensor computation for data analysis*. Springer, 2022.
- [17] J. D. Carroll and J.-J. Chang, "Analysis of individual differences in multidimensional scaling via an N-way generalization of "Eckart-Young" decomposition," *Psychometrika*, vol. 35, no. 3, pp. 283-319, 1970.
- [18] L. R. Tucker, "Some mathematical notes on three-mode factor analysis," *Psychometrika*, vol. 31, no. 3, pp. 279-311, 1966.
- [19] I. V. Oseledets, "Tensor-train decomposition," *SIAM Journal on Scientific Computing*, vol. 33, no. 5, pp. 2295-2317, 2011.
- [20] M. E. Kilmer and C. D. Martin, "Factorization strategies for third-order tensors," *Linear Algebra and its Applications*, vol. 435, no. 3, pp. 641-658, 2011.
- [21] A. Cichocki *et al.*, "Tensor networks for dimensionality reduction and large-scale optimization:

- Part 2 applications and future perspectives," *Foundations and Trends® in Machine Learning*, vol. 9, no. 6, pp. 431-673, 2017.
- [22] S.-Y. Chang and H.-C. Wu, "Tensor-based least-squares solutions for multirelational signals and applications," *IEEE Transactions on Cybernetics*, 2023.
- [23] Y. Qiu, G. Zhou, Q. Zhao, and S. Xie, "Noisy tensor completion via low-rank tensor ring," *IEEE Transactions on Neural Networks and Learning Systems*, vol. 35, no. 1, pp. 1127-1141, 2022.
- [24] W. Kong, F. Zhang, W. Qin, and J. Wang, "Low-Tubal-Rank tensor recovery with multilayer subspace prior learning," *Pattern Recognition*, vol. 140, p. 109545, 2023.
- [25] L. Lin *et al.*, "A 3D Multi-Scale Multi-Attention UNet for Automatic Hippocampal Segmentation," in *2021 7th Annual International Conference on Network and Information Systems for Computers (ICNISC)*, 2021: IEEE, pp. 89-93.
- [26] J. Shi *et al.*, "Dual dense context-aware network for hippocampal segmentation," *Biomedical Signal Processing and Control*, vol. 61, p. 102038, 2020.
- [27] Z. Yang, X. Zhuang, V. Mishra, K. Sreenivasan, and D. Cordes, "CAST: A multi-scale convolutional neural network based automated hippocampal subfield segmentation toolbox," *NeuroImage*, vol. 218, p. 116947, 2020.
- [28] M. Goubran *et al.*, "Hippocampal segmentation for brains with extensive atrophy using three-dimensional convolutional neural networks," *Human brain mapping*, vol. 41, no. 2, pp. 291-308, 2020.
- [29] H. Zhu *et al.*, "Dilated dense U-Net for infant hippocampus subfield segmentation," *Front. Neuroinform.*, vol. 13, p. 30, 2019.
- [30] D. Ataloglou, A. Dimou, D. Zarpalas, and P. Daras, "Fast and precise hippocampus segmentation through deep convolutional neural network ensembles and transfer learning," *Neuroinformatics*, vol. 17, no. 4, pp. 563-582, 2019.
- [31] E. Balboni *et al.*, "The impact of transfer learning on 3D deep learning convolutional neural network segmentation of the hippocampus in mild cognitive impairment and Alzheimer disease subjects," *Human Brain Mapping*, vol. 43, no. 11, pp. 3427-3438, 2022.
- [32] A. van Opbroek, H. C. Achterberg, M. W. Vernooij, M. A. Ikram, M. de Bruijne, and A. s. D. N. Initiative, "Transfer learning by feature-space transformation: A method for Hippocampus segmentation across scanners," *NeuroImage: Clinical*, vol. 20, pp. 466-475, 2018.
- [33] C. Mou *et al.*, "T2i-adapter: Learning adapters to dig out more controllable ability for text-to-image diffusion models," in *Proceedings of the AAAI Conference on Artificial Intelligence*, 2024, vol. 38, no. 5, pp. 4296-4304.
- [34] R. Zhang *et al.*, "Llama-adapter: Efficient fine-tuning of language models with zero-init attention," *arXiv preprint arXiv:2303.16199*, 2023.
- [35] X. L. Li and P. Liang, "Prefix-tuning: Optimizing continuous prompts for generation," *arXiv preprint arXiv:2101.00190*, 2021.
- [36] X. Chen, J. Liu, Y. Wang, M. Brand, G. Wang, and T. Koike-Akino, "SuperLoRA: Parameter-Efficient Unified Adaptation of Multi-Layer Attention Modules," *arXiv preprint arXiv:2403.11887*, 2024.
- [37] S.-Y. Liu *et al.*, "Dora: Weight-decomposed low-rank adaptation," *arXiv preprint arXiv:2402.09353*, 2024.
- [38] C. Si *et al.*, "FLoRA: Low-Rank Core Space for N-dimension," *arXiv preprint arXiv:2405.14739*, 2024.

- [39] D. J. Kopiczko, T. Blankevoort, and Y. M. Asano, "Vera: Vector-based random matrix adaptation," *arXiv preprint arXiv:2310.11454*, 2023.
- [40] S. Jie and Z.-H. Deng, "Fact: Factor-tuning for lightweight adaptation on vision transformer," in *Proceedings of the AAAI conference on artificial intelligence*, 2023, vol. 37, no. 1, pp. 1060-1068.
- [41] G. H. Golub and C. F. Van Loan, *Matrix computations*. JHU press, 2013.
- [42] U. Baid *et al.*, "The rsna-asnr-miccai brats 2021 benchmark on brain tumor segmentation and radiogenomic classification," *arXiv preprint arXiv:2107.02314*, 2021.
- [43] M. Boccardi *et al.*, "Training labels for hippocampal segmentation based on the EADC-ADNI harmonized hippocampal protocol," *Alzheimer's & Dementia*, vol. 11, no. 2, pp. 175-183, 2015.
- [44] D. W. Shattuck *et al.*, "Construction of a 3D probabilistic atlas of human cortical structures," *NeuroImage*, vol. 39, no. 3, pp. 1064-1080, 2008.
- [45] K. Jafari-Khouzani, K. V. Elisevich, S. Patel, and H. Soltanian-Zadeh, "Dataset of magnetic resonance images of nonepileptic subjects and temporal lobe epilepsy patients for validation of hippocampal segmentation techniques," *Neuroinformatics*, vol. 9, no. 4, pp. 335-346, 2011.
- [46] G. Luo *et al.*, "Towards efficient visual adaption via structural re-parameterization," *arXiv preprint arXiv:2302.08106*, 2023.
- [47] D. Lian, D. Zhou, J. Feng, and X. Wang, "Scaling & shifting your features: A new baseline for efficient model tuning," *Advances in Neural Information Processing Systems*, vol. 35, pp. 109-123, 2022.